

Manuscript version: Published Version

The version presented in WRAP is the published version (Version of Record).

Persistent WRAP URL:

<http://wrap.warwick.ac.uk/160646>

How to cite:

The repository item page linked to above, will contain details on accessing citation guidance from the publisher.

Copyright and reuse:

The Warwick Research Archive Portal (WRAP) makes this work by researchers of the University of Warwick available open access under the following conditions.

Copyright © and all moral rights to the version of the paper presented here belong to the individual author(s) and/or other copyright owners. To the extent reasonable and practicable the material made available in WRAP has been checked for eligibility before being made available.

Copies of full items can be used for personal research or study, educational, or not-for-profit purposes without prior permission or charge. Provided that the authors, title and full bibliographic details are credited, a hyperlink and/or URL is given for the original metadata page and the content is not changed in any way.

Publisher's statement:

Please refer to the repository item page, publisher's statement section, for further information.

For more information, please contact the WRAP Team at: wrap@warwick.ac.uk

System parameters of three short-period cataclysmic variable stars

J. F. Wild¹  ¹★ S. P. Littlefair,¹ R. P. Ashley,^{2,3} E. Breedt¹ ,⁴ A. J. Brown¹ ,¹ V. S. Dhillon^{1,5} ,
M. J. Dyer¹ ,¹ M. J. Green^{1,6} ,^{2,6} P. Kerry,¹ T. R. Marsh,² S. G. Parsons¹  and D. I. Sahman¹

¹Department of Physics and Astronomy, University of Sheffield, Sheffield S3 7RH, UK

²Astronomy and Astrophysics Group, Department of Physics, University of Warwick, Coventry CV4 7AL, UK

³Isaac Newton Group of Telescopes, Apartado de Correos 321, Santa Cruz de La Palma, E-38700, Spain

⁴Institute of Astronomy, University of Cambridge, Madingley Road, Cambridge CB3 0HA, UK

⁵Instituto de Astrofísica de Canarias, E-38205 La Laguna, Tenerife, Spain

⁶School of Physics and Astronomy, Faculty of Exact Sciences, Tel Aviv University, Tel Aviv 69978, Israel

Accepted 2021 November 5. Received 2021 November 3; in original form 2021 July 19

ABSTRACT

Using photometric ULTRACAM observations of three new short-period cataclysmic variables (CVs), we model the primary eclipse light curves to extract the orbital separation, masses, and radii of their component stars. We find donor masses of $0.060 \pm 0.008 M_{\odot}$, $0.042 \pm 0.001 M_{\odot}$, and $0.042 \pm 0.004 M_{\odot}$, two being very low-mass sub-stellar donors, and one within 2σ of the hydrogen burning limit. All three of the new systems lie close to the empirical evolutionary sequence that has emerged from observations of the last decade. We briefly re-evaluate the long-standing discrepancy between observed donor mass and radius data, and theoretical CV evolutionary tracks. By looking at the difference in the observed period at each mass and the period predicted by the modelled evolutionary sequences, we qualitatively examine the form of excess angular momentum loss that is missing from the models below the period gap. We show indications that the excess angular momentum loss missing from CV models grows in importance relative to gravitational losses as the period decreases. Detailed CV evolutionary models are necessary to draw more quantitative conclusions in the future.

Key words: techniques: photometric – eclipses – white dwarfs.

1 INTRODUCTION

Cataclysmic variable (CV) stars are binary systems, containing white dwarf primary stars, and low-mass companion stars (Hellier 2001). Generally, the white dwarf is the more massive of the two, but CVs with the majority of the system mass contained in the companion star are possible (Ritter & Kolb 2003). The two stars orbit close enough that the companion completely fills its Roche lobe and the outer layers of its envelope are gradually stripped from its surface, falling towards the white dwarf around which an accretion disc forms. The companion has its mass transferred to the primary, so is referred to as the donor star (e.g. Warner 1995).

CVs evolve from long to short orbital periods, driven by the contraction of the donor in response to mass-loss (Patterson 1984). For CVs with orbital periods less than 6 h, mass-loss is a consequence of angular momentum loss (AML) from the binary. AML in CVs is generally considered to result from two mechanisms: gravitational wave braking (Paczynski & Sienkiewicz 1981), and magnetic braking (Rappaport, Verbunt & Joss 1983). CVs with long periods, more than ~ 3 h, exhibit both magnetic braking and gravitational wave braking, but below this period magnetic braking appears to cease and the donor contracts to its equilibrium radius (Spruit & Ritter 1983; Davis et al. 2008). This causes the donor to detach from the Roche lobe and mass transfer stops, leading to a period gap where

CVs are not observed (Kolb, King & Ritter 1998; Hellier 2001; Knigge 2006). The stars move closer together through gravitational losses, until at ~ 2.2 h the donor reconnects with its Roche lobe (Davis et al. 2008) and mass transfer resumes as a short-period CV, though with a significantly reduced transfer rate (Paczynski & Sienkiewicz 1981; Rappaport, Joss & Webbink 1982; Kolb & Baraffe 1999). The CV eventually evolves through a period minimum when the thermal time-scale of the donor becomes comparable to its mass-loss time-scale. Once beyond the period minimum, the donor expands in response to mass-loss, allowing it to sustain mass transfer as it retreats and leading to a widening of the orbit (Paczynski & Sienkiewicz 1981; Rappaport et al. 1982; Knigge 2006).

The observed location of the period minimum has been difficult to reproduce in evolutionary models (see Zorotovic & Schreiber 2020 for a review of this history), and the most common explanation of this discrepancy is an extra source of AML over the traditional gravitational wave and magnetic losses (King & Kolb 1995; Knigge, Baraffe & Patterson 2011). The donor mass and radius are expected to be a valuable diagnostic for CV evolution, as they should trace the long-term average mass-loss of the system (Knigge et al. 2011). Observations have so far produced an evolutionary sequence with little scatter between donor mass and radius, or between donor mass and orbital period, implying that CVs quickly converge on a singular evolutionary path (McAllister et al. 2019).

* E-mail: jwild2@sheffield.ac.uk

Table 1. Summary of objects observed for this work. Given magnitudes are the approximate magnitudes out of eclipse observed in this work. T_0 and P are the ephemerides calculated in Section A5. Parallax (π) is as measured by *Gaia* DR2 (Lindegren et al. 2018; Luri et al. 2018; Gaia Collaboration 2016, 2018). N_{ecl} is the number of ULTRACAM eclipse observations used in this analysis.

System	RA	Dec.	T_0 , BJJD, TDB (err)	P_{orb} , days (err)	Approx. System Magnitude				π , mas	N_{ecl}
					u'	g'	r'	i'		
ASASSN-16kr	22:05:59.48	−34:14:33.9	58635.424328(3)	0.061285932(1)	19.1	19.5	19.8	20.1	6.230 ± 0.266	7
ASASSN-17jf	20:29:17.13	−43:40:19.8	58756.50523(1)	0.0567904(7)	20.7	20.1	20.3	–	3.494 ± 1.127	3
SSSJ0522-3505	05:22:09.67	−35:05:30.3	58799.52170(1)	0.06219343(1)	19.1	19.0	19.3	–	1.214 ± 0.323	3

A physically motivated solution for missing AML was proposed by King & Kolb (1995), in which angular momentum is lost as a consequence of mass transfer, and hence is called consequential AML, or CAML. Schreiber, Zorotovic & Wijnen (2016) suggest this is caused by mass ejection from nova outbursts, making AML a function of the white dwarf mass and accretion rate. With some tuning, this idea is able to solve three long-standing problems in CV evolution: low observed CV space density (e.g. Britt et al. 2015), the missing observations of systems below the period gap (Kolb 1993; Knigge 2006), and the observed high CV white dwarf masses (e.g. McAllister et al. 2019). However, there is not yet any direct evidence for this theory.

While promising, CAML is not the only potential extra source of AML. The CV field has long made the assumption that magnetic braking either fully, or almost fully, ceases at the period gap (McDermott & Taam 1989; Taam & Spruit 1989), leaving AML dominated by gravitational wave braking. However, it is unlikely that magnetic braking fully stops, and the strength of the remainder is unknown, only assumed to be negligible. Magnetic braking requires a strong magnetic field to couple to a significant stellar wind, but Garraffo et al. (2018) recently suggested that the structure of the magnetic field has a strong influence on its ability to drive a stellar wind, based on work by Taam & Spruit (1989). A more complex field will produce fewer open field lines, which are required to eject particles from the system and carry away angular momentum. Morin et al. (2010) find a wide range of field complexities in M dwarf stars, which is difficult to reconcile with the single, unified track driven by magnetic braking found by Knigge et al. (2011). However, as solitary low-mass stars with the high rotation rates of CV donors are extremely rare, the Morin et al. (2010) data do not cover the relevant region of the parameter space. It is feasible that the rapid rotation rates of CV donor stars stabilize the magnetic fields enough on thermal time-scales to produce the observed singular tracks. At least some residual magnetic braking is likely to be present below the period gap, but the question of how significant it is to the AML history of the CV remains.

The best probe for the AML history of a CV is the donor mass and radius evolution over orbital period (Knigge et al. 2011). However, direct measurements of masses and radii of the components of the very low-mass ratio CVs found at short periods are hard won and few in number, and McAllister et al. (2019) report only a handful of such systems. By modelling the eclipse of the white dwarf – a technique established by Wood & Crawford (1986) and further developed by Savoury et al. (2011) and McAllister et al. (2017) – we characterize three new CVs. Our method is described in Section 3

We characterize three recently identified CVs: ASASSN-16kr, ASASSN-17jf, and CRTS SSS11126 J052210-350530. These systems have been chosen for their short periods, and prior observations of each system are summarized below. Table 1 and Section 1.1 summarize their observational information.

1.1 Prior observations

1.1.1 ASASSN-16kr

ASASSN-16kr, a.k.a. MASTER J220559.40-341434.9, was discovered by the All-Sky Automated Survey for Supernovae (ASASSN) on 2016 September 11, and observed by the MASTER network on the 19th (ATel #9509 and #9510), both at ~ 14 th magnitude. Initially classified as an SS Cyg type object due to its low outburst amplitude (vsnet-alert #20189), subsequent observations confirmed eclipses and superhumping behaviour (vsnet alerts #20190, #20196, #20206; Kato et al. 2017).

Time-resolved photometry detected superhumps and eclipses, and Kato et al. (2017) calculated an orbital period of 0.0612858 ± 0.0000003 d, and a superhump period of 0.061999 ± 0.000067 d. Kato et al. (2009) demonstrated that superhump periods vary systematically, and can be categorized into stages: stage A, an initial growth stage with a long period; stage B, a developed stage with a varying period; and stage C, with a shorter and more constant period. This system is noted by Kato et al. (2017) as being in the transition from stage B to stage C, though this is noted as possibly being due to a suspect measurement at the start of the outburst they observed.

1.1.2 ASASSN-17jf

ASASSN-17jf was confirmed as eclipsing by Berto Monard (vsnet #21257) between 2017 July 14 and 17. The system was initially observed with a mean unfiltered magnitude of ~ 15.5 outside eclipse, with an eclipse depth of ~ 1 magnitude. From these observations, an orbital period of 0.0578 ± 0.0003 d, and a rough superhump period of 0.0565 d was derived.

1.1.3 CRTS SSSJ0522-3505 J052210-350530

CRTS SSSJ0522-3505 J052210-350530, hereafter SSSJ0522-3505, was first observed by the CRTS on 2005 February 28, and as recently as 2019 November 11 (Drake et al. 2008). These data show high variability, and outbursts ~ 6 months apart. High time resolution light curves taken by Paterson et al. (2019) show an eclipse depth of ~ 1.5 mag and an orbital period of 0.0622 ± 0.0005 d.

2 OBSERVATIONS AND DATA REDUCTION

Observations were taken with ULTRACAM (Dhillon et al. 2007), mounted on the 3.58-m New Technology Telescope (NTT) in La Silla, Chile. ULTRACAM is a three-colour camera capable of observing these ~ 20 th magnitude systems at a time resolution of a few seconds, with a signal/noise ratio high enough to resolve the various components of the eclipse.

Table 2. Journal of Observations. Each eclipse is imaged in three colours simultaneously by ULTRACAM mounted on the NTT. SDSS-like filters are denoted by subscript *reg*, and upgraded, higher throughput filters are denoted by subscript *sup*; see Section A2 for details.

System	Date	Start time UTC	Stop time UTC	T_{ecl} BJMD, TDB, (err)	Ecl. N ^o	Filters	Flux standard used	Airmass
ASASSN-16kr	2018-10-13 [†]	02:34:58	03:15:43	58404.131217(3)	−3774	$u_{\text{reg}}, g_{\text{reg}}, r_{\text{reg}}$	G 27-45	1.04-1.10
	2018-10-16 [†]	04:25:49	04:59:32	58407.1955(2)	−3724	$u_{\text{reg}}, g_{\text{reg}}, r_{\text{reg}}$	G 27-45	1.33-1.50
	2018-10-17 [†]	02:24:23	04:26:57	58408.114806(4), 58408.176(1)	−3709, −3708	$u_{\text{reg}}, g_{\text{reg}}, r_{\text{reg}}$	G 27-45	1.05-1.35
	2019-09-27	23:56:59	00:27:17	58754.012610(3)	1935	$u_{\text{sup}}, g_{\text{sup}}, r_{\text{sup}}$	SA 114 548	1.11-1.17
	2019-09-29	00:48:44	01:37:34	58755.054468(3)	1952	$u_{\text{sup}}, g_{\text{sup}}, r_{\text{sup}}$	SA 114 548	1.02-1.06
ASASSN-17jf	2019-09-30	03:21:59	04:02:34	58756.157613(4)	1970	$u_{\text{sup}}, g_{\text{sup}}, r_{\text{sup}}$	SA 114 548	1.03-1.09
	2019-09-28	01:41:39	03:04:00	58754.12003(2)	−42	$u_{\text{sup}}, g_{\text{sup}}, r_{\text{sup}}$	SA 114 548	1.05-1.16
	2019-09-30	02:16:18	02:46:29	58756.10769(1)	−7	$u_{\text{sup}}, g_{\text{sup}}, r_{\text{sup}}$	SA 114 548	1.10-1.14
SSSJ0522-3505	2019-10-01	04:08:56	04:38:37	58757.18671(1)	12	$u_{\text{sup}}, g_{\text{sup}}, r_{\text{sup}}$	SA 114 548	1.40-1.55
	2019-09-29	08:12:53	09:00:37	58755.364361(6)	−710	$u_{\text{sup}}, g_{\text{sup}}, r_{\text{sup}}$	SA 114 548	1.01-1.05
	2019-10-01	08:01:32	08:42:20	58757.35456(1)	−678	$u_{\text{sup}}, g_{\text{sup}}, r_{\text{sup}}$	SA 114 548	1.02-1.06
	2020-01-29	04:07:50	05:02:36	58877.20128(5)	1249	$u_{\text{sup}}, g_{\text{sup}}, i_{\text{sup}}$	BD -210910	1.19-1.39

[†] Calibration of these data use the uncorrected standard magnitudes provided in Smith et al. (2002), without the colour corrections described in Sections A2 and A4.

Observations were taken on several nights in four observing runs spanning from 2018 October 13 to 2020 January 29. Table 2 summarizes these observations. A full discussion of calibrating the data is given in Appendix A. Briefly, instrument signature removal and aperture photometry was performed using the HiPERCAM pipeline software,¹ and flux calibration used nearby comparison stars in conjunction with known flux secondary standards.

3 MODELLING THE CV

To determine the system parameters for the three CVs in this study, the eclipse light curves were modelled. This method is more frequently applicable in CVs than the more traditional approach of using spectroscopic eclipsing binaries, since the donor star is rarely directly visible. Compared to using the superhump period excess to estimate the mass ratio (Patterson et al. 2005; Knigge 2006), light-curve modelling requires few assumptions. However, it does require precise alignment of the system and so is not possible for a large fraction of CVs.

Several excellent discussions of the technique exist in the literature (e.g. Wood & Crawford 1986; Savoury et al. 2011; McAllister et al. 2017, 2019), though we summarize key elements of the approach here. Four assumptions are made: the bright-spot originates where a ballistic trajectory from the donor meets the outer edge of the accretion disc, the white dwarf obeys a theoretical mass–radius relationship, the white dwarf is unobscured by the accretion disc or other sources of intra-system material, and the donor exactly fills its Roche lobe. Most of these assumptions are considered robust, though the visibility of the white dwarf has been called into question by Spark & O’Donoghue (2015). Since the white dwarf radius is inferred from the duration of ingress/egress, complicating structures like a surface layer of accreted material could lead to an inaccurate white dwarf radius, and hence mass. However, system parameters from light-curve modelling agree with other methods (Tulloch, Rodríguez-Gil & Dhillon 2009; Copperwheat et al. 2012; Savoury et al. 2012), suggesting that this is not normally an issue. The model for one eclipse is described by 18 parameters:

- (i) white dwarf, disc, bright-spot, and donor fluxes, $F_{(\text{WD, disc, BS, donor})}$;
- (ii) mass ratio, $q = \frac{M_{\text{donor}}}{M_{\text{WD}}}$;
- (iii) white dwarf eclipse width, in units of phase, $\Delta\phi$;
- (iv) scaled white dwarf radius, R_{WD}/a ;
- (v) white dwarf limb darkening coefficient, u_{ld} ;
- (vi) scaled outer disc radius, R_{disc}/a ;
- (vii) disc surface profile exponent;
- (viii) seven parameters describing the bright-spot behaviour;
- (ix) an eclipse phase offset, ϕ_0 ;

where a is orbital separation between the white dwarf and donor star. The seven bright-spot parameters describe its brightness profile and beaming, location on the rim of the accretion disc, and emission angle, but are not physically motivated. For details, see Savoury et al. (2011).

In addition, there are three nuisance parameters, which set the time-scale and amplitude of a Gaussian process that describes flickering. These parameters are common to all eclipses for a system.

3.1 Light-curve fitting procedure

We extend the light-curve fitting model used by McAllister et al. (2019), adopting a hierarchical approach to slightly reduce model complexity.

Changes in the disc radius and brightness profile, and bright-spot parameters can mean that the same CV has a significantly different eclipse light curve at different times, making it difficult to justify averaging together many eclipses, as features can become smeared out and uninformative. In the worst-case scenario, all 18 parameters would be independently variable for each eclipse, in each band. However, by sharing some parameters between eclipses and bands, this large number of free parameters is slightly reduced, and the posterior of some parameters can be informed by multiple eclipses. McAllister et al. (2017) share $q, R_{\text{WD}}/a$, and $\Delta\phi$ between eclipses, and we extend that concept by organizing the model into a hierarchical tree structure, a schematic of which is shown in Fig. 1.

The top level of the model provides the core parameters, which are unchanging between all observing bands and constant across our observations: $q, R_{\text{WD}}/a$, and $\Delta\phi$. We assume the white dwarf and

¹ <http://www.vikdhillon.staff.shef.ac.uk/hipercam/resources.html>

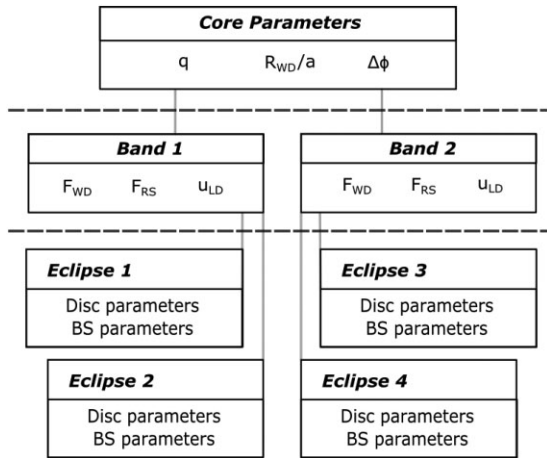


Figure 1. The hierarchical structure of the light-curve model. Parameters are inherited downwards, to produce an eclipse at the ‘leaves’ of the tree, e.g. Eclipse 3 inherits the parameters of Band 2, which in turn inherits the Core parameters. $F_{WD,RS}$ represent the fluxes of the white dwarf and donor star, and U_{LD} is the limb darkening coefficient of the white dwarf.

donor fluxes do not change on the time-scale of our observations, and so these variables, along with the limb darkening coefficient of the white dwarf, are shared between all eclipses observed with the same filters. The bottom level holds parameters that can vary quickly enough to change between eclipses, i.e. parameters describing the accretion disc and bright-spot. By handling parameters this way, we maximize the amount of data informing important variables, for example, white dwarf fluxes and q . We also somewhat reduce the number of free parameters, which aids slightly in model fitting, but the chief justification for the hierarchical approach is that it ensures consistency between eclipses – something not guaranteed when fitting eclipses individually.

As more eclipses are added, the number of dimensions in parameter space that must be explored increases. For illustration, the model for ASASSN-17jf has 3 eclipses across 3 bands, plus 3 Gaussian process parameters, resulting in 87 free parameters that must be optimized simultaneously. To find the most likely set of light-curve parameters in this very large space, an ensemble Markov chain Monte Carlo (MCMC) fitting code was used. The MCMC uses the `emcee` implementation of an ensemble sampler and parallel tempering (Foreman-Mackey et al. 2013) to aid convergence to a global minimum despite the large parameter space, as described in McAllister et al. (2019).

3.2 Conversion to physical parameters

By capturing eclipses in multiple filters, preferably simultaneously, we can extract white dwarf colours from the eclipse fitting. Model white dwarf cooling tracks from Bergeron, Wesemael & Beauchamp (1995) list the absolute magnitudes of white dwarfs of a given T_{eff} and $\log(g)$, and we fit these to the observed white dwarf fluxes, along with two nuisance parameters: parallax, π ; and interstellar extinction, $E(B-V)$. For $E(B-V)$, the IRSA extinction maps were used to inform the prior, providing a maximum allowed value; uniform priors between zero and the maximum $E(B-V)$ were used. A Gaussian prior on π based on *Gaia* data was used (Lindgren et al. 2018; Luri et al. 2018; Gaia Collaboration 2016, 2018). The priors used for $\log(g)$ and T_{eff} were more complicated, and are outlined in Section 4.1.

To calculate SI values for system parameters, we employ the technique developed by Wood & Crawford (1986). White dwarfs follow well-understood cooling tracks that relate the stars’ T_{eff} , R_{WD} , and M_{WD} . We have an estimate for T_{eff} as described above, so for an initial guess of the white dwarf mass, the cooling track provides a corresponding white dwarf radius. The relations we use are taken from Wood (1995) and Panei, Althaus & Benvenuto (2000), which each cover a different range of M_{WD} .

Eclipse modelling gives us a mass ratio, so the M_{WD} guess can be used to calculate the total mass of the system, M_{T} . M_{T} and P , via Keplers’ third law, gives the orbital separation. Using the R_{WD}/a from eclipse modelling, R_{WD} can be calculated. If the original guess for M_{WD} is correct, the resulting R_{WD} will be consistent with the value obtained from the cooling track, allowing the correct white dwarf mass to be found.

Once the white dwarf mass has been found, we can calculate a and re-scale the parameters produced by eclipse modelling to SI units. The following list of important system parameters is produced:

- (i) white dwarf mass and radius, $M_{\text{WD}}, R_{\text{WD}}$
- (ii) the $\log(g)$ corresponding to (i)
- (iii) white dwarf T_{eff}
- (iv) donor mass and radius, $M_{\text{donor}}, R_{\text{donor}}$
- (v) white dwarf – donor separation, a
- (vi) orbital velocities, $k_{\text{WD}}, k_{\text{donor}}$

Note that *two* values of $\log(g)$ are produced in this process, one from fitting the white dwarf fluxes to model atmospheres, and one from combining the T_{eff} estimate with light-curve parameters.

4 RESULTS

For all three systems eclipse modelling gave good results, each light curve being well modelled with small residuals – for a catalogue of the fits, see Appendix B, figures B3, B4, B11 and B12. Figure 2 is provided in the main text as an example lightcurve fit. The Gaussian processes describing flickering in the systems were consistent with little to no variability, as almost all the scatter in the flux residuals could be fully described by the uncertainty in flux measurement.

4.1 White dwarf atmosphere fits

The two values of $\log(g)$ produced by modelling – the first from fitting the white dwarf fluxes to model atmospheres, and the second from combining T_{eff} and P with the light-curve parameters – did not fall within 1σ of each other in any of our systems. In ASASSN-17jf and SSSJ0522-3505, the white dwarf atmosphere fit converged close to the minimum surface gravity allowed by the coverage of our models, $\log(g) = 7.0$. The second $\log(g)$, from light-curve fitting, indicated values for each system of 8.10 ± 0.04 and 8.30 ± 0.03 , respectively. When analysing ASASSN-16kr, flux fitting gave a more reasonable $\log(g) = 8.21 \pm 0.13$, but the second $\log(g)$ still gave a significantly higher $\log(g) = 8.59 \pm 0.03$, a difference of $\sim 3\sigma$.

This is concerning, as the two $\log(g)$ should be consistent with one another for each system. Comparison of our measured white dwarf colours to the Bergeron et al. (1995) model grids in Figs 3–5, reveals that the measured colours of the white dwarfs lie outside the colour space of the models. This is the origin of the discrepancies in $\log(g)$ obtained with the two methods for ASASSN-17jf and SSSJ0522-3505, but ASASSN-16kr appears consistent with the leftmost cooling track. However, the observed flux of a white dwarf of this radius is too high for the observed *Gaia* parallax, pushing the model fits to smaller, higher gravity model atmospheres.

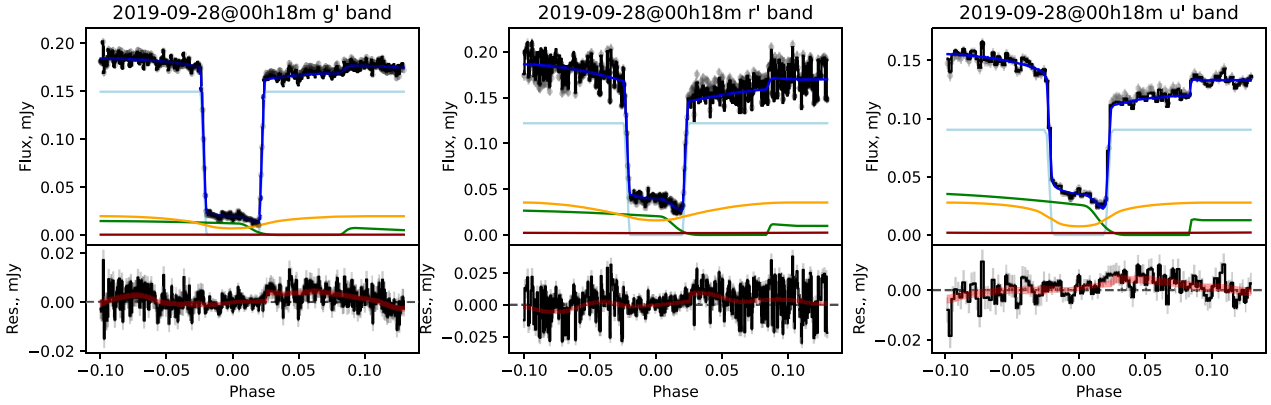


Figure 2. ASASSN-16kr example light-curve models. *Top:* grey points are the observed flux; black line is the observed flux, with the mean Gaussian process sample subtracted; the dark blue line is the mean light-curve model, and the blue band is the standard deviation on this in the MCMC chain. The components of the model are also shown: the light blue line is the white dwarf flux, green line is the bright-spot, orange line is the disc, and the red line is the donor. *Bottom:* The residuals between the data and model are plotted as the black line, with grey error bars. The Gaussian process 1σ region is shown as a red band. A catalogue of all such fits in this work is given in Appendix B.

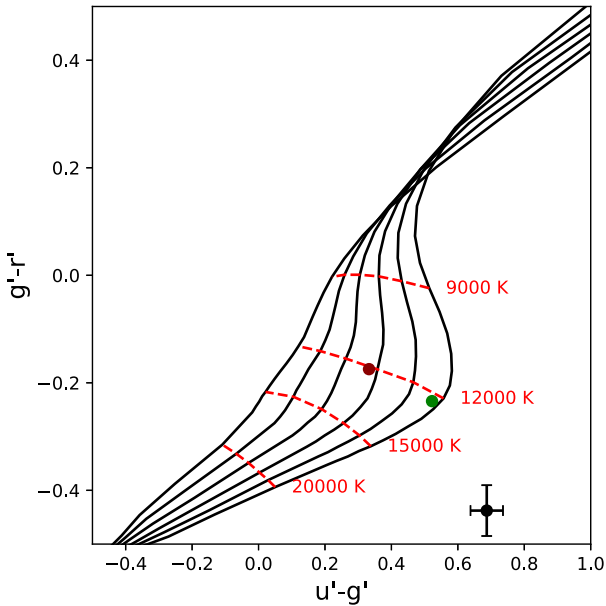


Figure 3. The white dwarf model atmosphere fits for ASASSN-17jf. Green circle: Best fit with uniform prior on $\log(g)$. Red circle: Best fit with the prior $\log(g) = 8.10 \pm 0.04$. The observations are shown as the black point and error bars. Solid black lines are white dwarf model cooling tracks, increasing in $\log(g)$ to the left. Red dashed lines are isothermal tracks for different $\log(g)$.

A possible cause for this issue would be an error in photometric calibration, causing a corresponding error in white dwarf fluxes. We do not believe this to be a problem, for the reasons explained in Section A4. Inspection of the figures in Appendix B also rules out poor light-curve fits as the cause of this problem. The most plausible explanation for the fact that our measured white dwarf fluxes do not lie inside the model grids, is that the change in brightness during white dwarf ingress/egress is contaminated by an additional source of light, for example a boundary layer close to the white dwarf surface. The implications of this for our system parameters is discussed in Section 5.1.

That our white dwarf colours do not lie on the model grids also raises questions about the accuracy of our white dwarf temperatures. To try and quantify the impact on T_{eff} we performed two additional fits

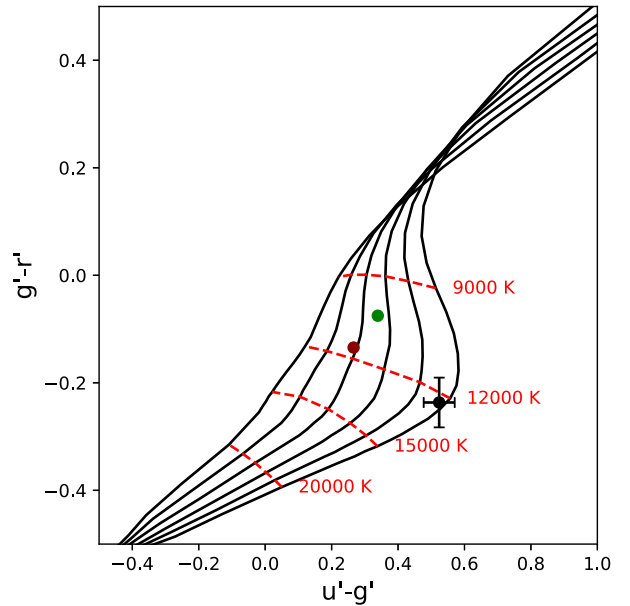


Figure 4. The white dwarf model atmosphere fits for ASASSN-16kr. The red circle is the best fit with a prior of $\log(g) = 8.52 \pm 0.02$. Symbols are the same as Fig. 3.

to the white dwarf fluxes. In one approach, we fit fluxes in all bands, but used a Gaussian prior on $\log(g)$ using the estimate from the light-curve modelling. In a second approach, we fit the white dwarf flux in each band independently using the same prior on $\log(g)$ and the *Gaia* prior on π . Since these independent fits use no colour information, $E(B-V)$ is only constrained by the prior, but we retain it as a nuisance parameter and marginalize our T_{eff} estimate over $E(B-V)$. Fig. 6 shows the T_{eff} posteriors from the individual fits for the three systems.

From Fig. 6, we can see that there is little sign of a consistent discrepancy over the three observed CVs. The u' band in ASASSN-16kr and SSSJ0522-3505 suggests a cooler temperature than the other bands, but lies in between the r' and g' in ASASSN-17jf.

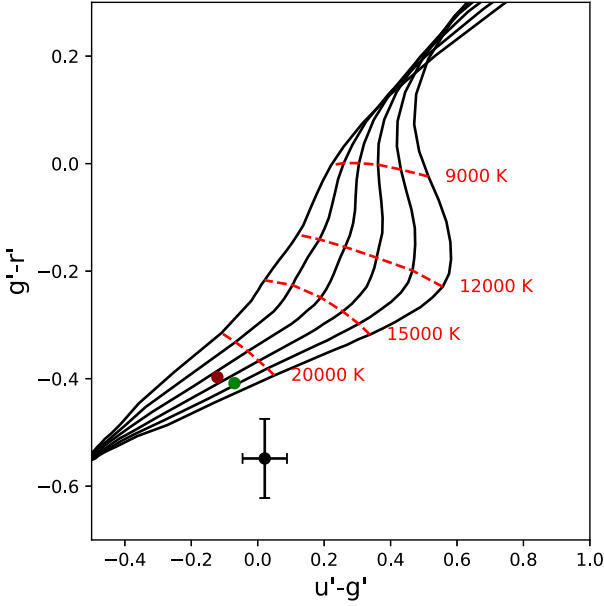


Figure 5. The white dwarf model atmosphere fits for SSSJ0522-3505. The red circle is the best fit with a prior of $\log(g) = 8.28 \pm 0.04$. Symbols are the same as Fig. 3.

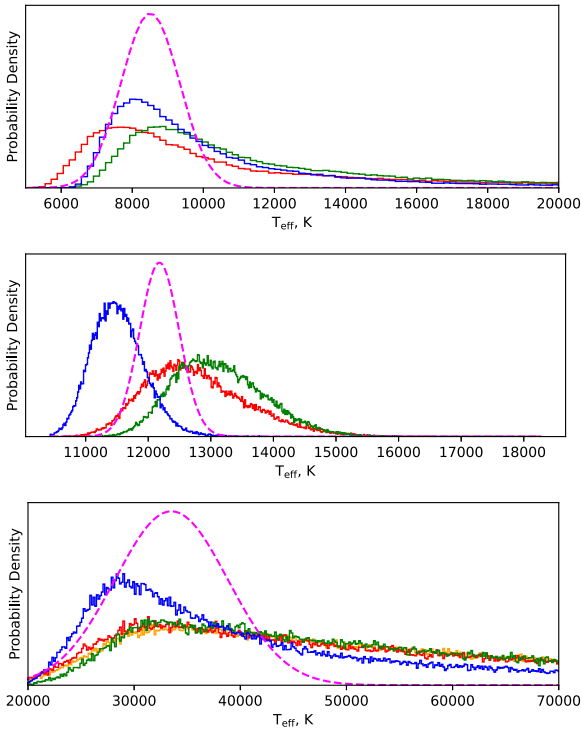


Figure 6. The result of fitting white dwarf model atmospheres to each photometric band independently. Blue solid line: u' band, green solid line: g' band, red solid line: r' band. The joint distribution between all bands is characterized in each case by the best-fitting Gaussian (magenta dashed lines). *Top:* ASASSN-17jf, joint $T_{\text{eff}} = 8330 \pm 780$ K; *Middle:* ASASSN-16kr, joint $T_{\text{eff}} = 12150 \pm 300$ K; *Bottom:* SSSJ0522-3505, joint $T_{\text{eff}} = 33300 \pm 5200$ K.

4.1.1 White dwarf temperature fits

Each approach gives a different distribution for T_{eff} . To avoid confusion, we do not report the results of each individual fit, but summarize the overall temperature ranges for each system.

ASASSN-16kr T_{eff} estimates ranged from 10 200 to 12 150 K, and ASASSN-17jf estimates from 8330 to 12 710 K. The SSSJ0522-3505 fits that used all four observed fluxes both converged on ~ 22 700 K, but the single-flux fits all resulted in wide posterior distributions covering 25 000–90 000 K, with very weak peaks in the ~ 30 000–50 000 K range, seen in Fig. 6.

In all three systems, the figures we report in Table 3 are the T_{eff} produced by the constrained $\log(g)$ fit with all fluxes simultaneously. The $\log(g)$ reported are the values found from the light-curve parameters.

4.2 System parameters

We note that the effect of the uncertain white dwarf temperatures on the system parameters, such as M_{wd} , is negligible. For example, increasing T_{eff} for ASASSN-17jf from 8000 to 12 000 K only changes M_{WD} by $0.001 M_{\odot}$, compared to our statistical uncertainty of $0.031 M_{\odot}$. Even a large uncertainty in T_{eff} only has a minor impact on the system parameters; for example, a change in the WD temp for SSSJ0522-3505 from 10 000 to 20 000 K only changes M_{WD} by $0.02 M_{\odot}$, comparable with the measurement uncertainty. The system parameters are reported in Table 3.

ASASSN-16kr has a recorded superhump period, and now also a robust q measurement. It can therefore be used to calibrate the superhump period excess, ϵ versus q relationship, as done in McAllister et al. (2019), though with a more extreme mass ratio system than was available to them. The system was not confidently classed as exhibiting stage B or C stage superhumps, so we look at the results for both stages. Assuming the CV was in stage B, we calculate $q_B = 0.059 \pm 0.007$; assuming stage C and using the relevant relation from McAllister et al. (2019), we calculate $q_C = 0.068 \pm 0.012$. In both cases, the estimated $q_{B,C}$ is $\sim 2\sigma$ higher than the observed value of $q = 0.044 \pm 0.002$. While a 2σ difference is not a highly significant discrepancy, this may be preliminary evidence that the $\epsilon - q$ relation may over estimate q for CVs at short periods, which has been suspected for some time (Pearson 2007; Knigge et al. 2011).

5 DISCUSSION

All three systems were candidate post-period minimum systems based on their periods and preliminary eclipse data; none show a prominent bright-spot (indicative of a low-mass transfer rate), or significant donor flux (implying a dim donor). As a result of this work, ASASSN-16kr and SSSJ0522-3505 are confirmed as having evolved through the period minimum and now have sub-stellar donors, and ASASSN-17jf lies in the period minimum region of Fig. 7. Additionally, all three white dwarf masses we derive in this analysis fall within the range of CV white dwarf masses observed by Pala et al. (2020), of $\langle M_{\text{WD}} \rangle = 0.83 \pm 0.17 M_{\odot}$, significantly higher than the pre-CV DA white dwarf mass of only $0.66 \pm 0.15 M_{\odot}$ (McCleery et al. 2020). Table 3 summarizes the results for each system.

5.1 Are we correct in assuming an unobscured white dwarf?

As discussed in Section 4.1.1, we believe the white dwarf colours could differ from model grids because the white dwarf ingress/egress is contaminated by an additional source of light, perhaps a boundary

Table 3. The system parameters found for each system in this work.

System name:	ASASSN-16kr	ASASSN-17jf	SSSJ0522-3505
M_{WD}/M_{\odot}	0.952 ± 0.018	0.669 ± 0.031	0.760 ± 0.023
R_{WD}/R_{\odot}	0.0083 ± 0.0002	0.0120 ± 0.0004	0.0112 ± 0.0003
$M_{\text{donor}}/M_{\odot}$	0.042 ± 0.001	0.060 ± 0.008	0.042 ± 0.004
$R_{\text{donor}}/R_{\odot}$	0.105 ± 0.002	0.112 ± 0.004	0.105 ± 0.004
q	0.044 ± 0.002	0.085 ± 0.006	0.055 ± 0.003
a/R_{\odot}	0.653 ± 0.005	0.567 ± 0.009	0.614 ± 0.007
i	86.4 ± 0.4	83.7 ± 0.5	83.8 ± 0.3
K_{WD} , km s^{-1}	22.7 ± 1.5	39.5 ± 4.2	26.0 ± 1.8
K_{donor} , km s^{-1}	515 ± 3	462 ± 5	470 ± 4
T_{eff} , kK	10 – 12	8 – 13	~25
$\log(g)$, cgs	8.55 ± 0.03	8.15 ± 0.05	8.22 ± 0.04

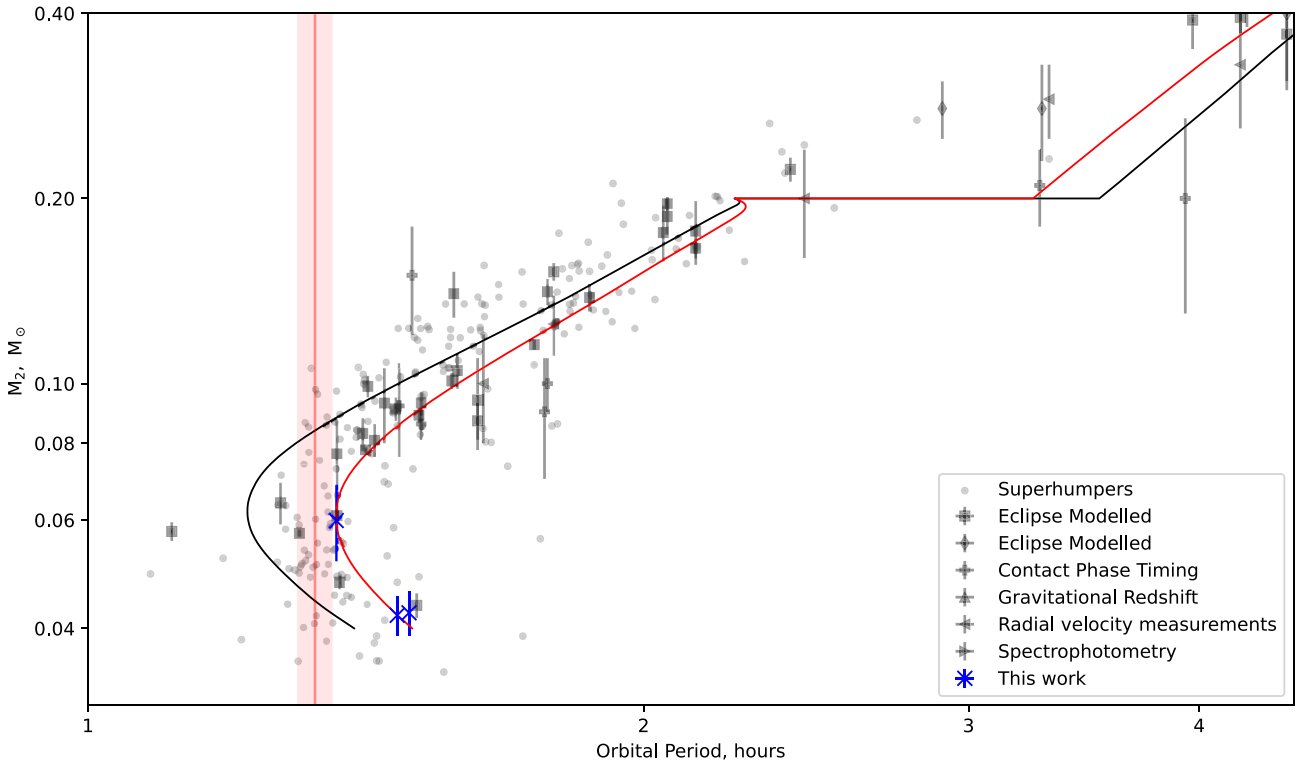


Figure 7. Donor evolution tracks – note that both axes are scaled logarithmically. Solid black line: the standard donor sequence from Knigge et al. (2011), solid red line: the ‘optimal’ donor track from Knigge et al. (2011). Vertical red line and shaded region: average period and 1σ region of these observed data between 76 and 82 min, 79.6 ± 1.6 min. Symbols denote the method used to analyse the data. **EM(U)**: Eclipse modelling with ULTRACAM, ULTRASPEC, or HiPERCAM data. **EM**: Eclipse modelling with other instruments. **CPT**: Contact phase timing. **GR**: Gravitational redshift. **RV**: Radial velocity measurement. **SM**: Spectrophotometric modelling. Blue crosses are the systems from this work.

layer close to the surface. If the eclipse we see is polluted by some other feature, our modelling will be wrong in two key elements: the colours we compare to model atmospheres will be incorrect, and the ingress and egress durations that constrain the white dwarf radius will not be accurate. Spark & O’Donoghue (2015) conducted a study into the validity of assuming a pure white dwarf, comparing CV eclipse observations with white dwarfs with and without a few types of surface features such as boundary layers on the white dwarf, hot spots, or an optically thick or thin equatorial belt. These features are revealed by a departure from symmetry between the white dwarf ingress and egress, but care must be taken not to confuse the flickering component of the CV with the signature of surface features.

Unfortunately, detecting a surface layer or hotspot on the white dwarf requires both a high time resolution and high signal-to-noise ratios. Spark & O’Donoghue (2015) make use of SALTICAM data at a cadence of 0.15 s, but our observations have a $\sim 3\text{--}4$ s exposure time and have lower signal-to-noise. We are unable to measure the eclipse precisely enough to make claims about the nature of the white dwarf’s surface. The three systems of this work are prime candidates to search for WD eclipse asymmetries, as the issue of flickering corrupting the white dwarf ingress/egress derivative is largely mitigated; all three have little to no flickering present. Future observations at higher cadence would open the possibility of examining the surfaces of these white dwarfs,

though a large telescope will necessary due to the faintness of the systems.

5.2 The hot white dwarf of SSSJ0522-3505

The effective temperature of white dwarfs in short-period CVs is typically $\sim 10\,000$ K (Pala et al. 2017), but our observed colours of SSSJ0522-3505 indicate a much hotter T_{eff} of $\sim 25\,000$ K, which we believe to be accurate as the system’s observations are dominated by the white dwarf flux, and show roughly the same eclipse depth in the r' , g' , and u' bands, that would not be consistent with a lower white dwarf temperature.

Our measured effective temperature could be wrong, either as a result of poor flux calibration (see Section A4) or because the ingress/egress fluxes do not represent the fluxes of the white dwarf photosphere, as discussed in section 5.1. However, our measured temperature is $\sim 10\,000$ K hotter than expected, and we do not believe these effects have introduced an error of this magnitude. As support for this, we note that Pala et al. (2017) find that white dwarf temperatures from ultraviolet (UV) spectroscopy typically agree with those measured from eclipse light curves to within ~ 1000 K. Therefore, we explore below reasons why the white dwarf temperature in SSSJ0522-3505 might be unusually hot, but note that UV spectroscopy to confirm the white dwarf temperature is highly desirable.

The white dwarf in a CV is thought to settle at an equilibrium temperature, where radiative heat loss is balanced with two energy sources: energy released by infalling material, and a low level of ‘simmering’ nuclear fusion in the white dwarf envelope (Townsend & Bildsten 2003, 2004), but there are several reasons that this white dwarf may be temporarily out of equilibrium. There is no reason, though it is unlikely, that a CV cannot form from a main-sequence star with a brown dwarf companion, to produce a young CV with a low-mass donor and a white dwarf still cooling from its formation temperature. Once the donor has reconnected with its Roche lobe, it would rejoin the normal CV evolution track and otherwise behave as a normal CV, with a normal accretion rate but a younger, hotter white dwarf than is typical.

A recent dwarf nova outburst was observed in this system in 2011, and could have produced a temporary boost to T_{eff} . During these events, the disc enters a hot, optically thick state, and the infall rate on to the white dwarf is greatly increased (Osaki 1996), releasing a significant amount of energy and heating the white dwarf surface. This is only the most recent *observed* outburst, as there is a gap in observations between 2013 and 2019 during which any outburst events would have gone unrecorded. This may be important, as recent X-ray observations of another post-period minimum system, OV Bootis (Schwope, Worpel & Traulsen 2021), shows that the WD temperature is increased to $23\,000$ K, 5 months after outburst, 9000 K hotter than its T_{eff} prior to outburst. The increase in temperature can be long lasting; detailed observations of GW Lib have shown its WD is still 3000 K hotter than equilibrium 8 yr post-outburst (Szkody et al. 2016). Another possibility is a recent classical nova – thermonuclear runaway in an accreted surface layer on the white dwarf – which would temporarily heat the white dwarf beyond its equilibrium temperature (Starrfield, Iliadis & Hix 2016), giving the impression of a hotter white dwarf than expected, though a classical nova resulting in such a strong heating effect would be surprising.

If, however, we assume the white dwarf is in thermal equilibrium, T_{eff} can be used to estimate the long-term accretion rate of the system (Townsend & Gänsicke 2009). If our modelled T_{eff} of SSSJ0522-3505 is both accurate and driven by accretion, it would correspond to

$\dot{M}_{\text{WD}} = 6 \pm 2 \times 10^{-10} M_{\odot} \text{yr}^{-1}$, compared to typical accretion rates of $\sim 10^{-11} M_{\odot} \text{yr}^{-1}$ for CVs in the post-period minimum regime (Pala et al. 2017). While high, a mass accretion rate of $10^{-10} M_{\odot} \text{yr}^{-1}$ is not incompatible with the presence of dwarf nova outbursts in SSSJ0522-3505, since a hot, optically thick accretion disc would require an accretion rate of order $10^{-8} M_{\odot} \text{yr}^{-1}$ (Hameury et al. 1998) to be stable on long time-scales.

5.3 Comments on the state of understanding AML in CVs

In order to qualitatively evaluate missing AML we examine the period *excess*, $P_{\text{ex}} = P_{\text{obs}} - P_{\text{model}}$, where P_{model} is the period predicted by the Knigge et al. (2011) track with only $1x$ gravitational braking below the period gap, interpolated across M_{donor} . P_{obs} is the observed period. To determine P_{ex} from an estimate of P_{obs} , M_{donor} , we sample from a Gaussian distribution based on the observed mean and standard deviation of M_{donor} and interpolate the evolutionary tracks to get a corresponding P_{model} distribution. As P_{model} is very sensitive to M_{donor} , the P_{model} error dominates the uncertainty in P_{ex} . A positive P_{ex} tells us the model is missing AML, and a negative P_{ex} indicates a model that has too much AML, relative to an observation.

Our reported P_{ex} should be treated with caution, and is only provided as an illustrative parameter. The validity of P_{ex} is vulnerable on two key systematic biases; the validity of P_{model} , and the inherent physical variation of the CV population.

CVs may follow inherently different evolutionary tracks due to differences in donor metallicity (Stehle, Kolb & Ritter 1997; Harrison 2016), white dwarf mass (Knigge 2006), and the age of the donor when it first contacts the Roche lobe (Howell 2001). A population-wide scatter in this parameter space is not captured in the Knigge et al. (2011) model, which uses fixed values for these variables, but justification for the adopted values are given (Knigge 2006; Knigge et al. 2011). If any individual system deviates from the adopted values in the models of Knigge et al. (2011) then P_{ex} for that system will be influenced by these differences as well as any extra AML. However, conclusions about P_{ex} drawn from the population at large should remain robust, as long as the population does not differ systematically from the values adopted in the models. The white dwarf mass used by Knigge et al. (2011) is somewhat lower than more recent observations suggest, using $M_{\text{WD}} = 0.75 M_{\odot}$ versus the more recent value of $M_{\text{WD}} = 0.83 \pm 0.17 M_{\odot}$ (Pala et al. 2020). Modelling will be necessary to properly characterize the effect of this change on the donor evolutionary tracks, as this will affect both the size of the Roche lobes, and the rate of gravitational wave AML. However, other CV models suggest that the effect will be small; at most around 2 min (Goliash & Nelson 2015).

More seriously, P_{ex} is only an accurate measure of additional AML, if the underlying donor physics in the model are correct. For example, if the models incorrectly predict the mass of systems in the period gap, this can have a large effect on P_{ex} . In the models of Knigge et al. (2011), this mass is fixed at the empirically derived value of $0.2 M_{\odot}$. Observations of superhumping and eclipsing CVs suggest that period gap occurs at donor masses of $0.20 \pm 0.02 M_{\odot}$ (Knigge 2006). Using model tracks with lower or higher masses for the donor mass of the period gap would change the absolute value of P_{ex} . However, the broad trend in P_{ex} will again be unchanged.

The result is plotted in Fig. 8. We fit the data with a straight line, and as the data have significant uncertainty in both axes, we minimize the sum orthogonal distance from the data (Hogg, Bovy & Lang 2010).

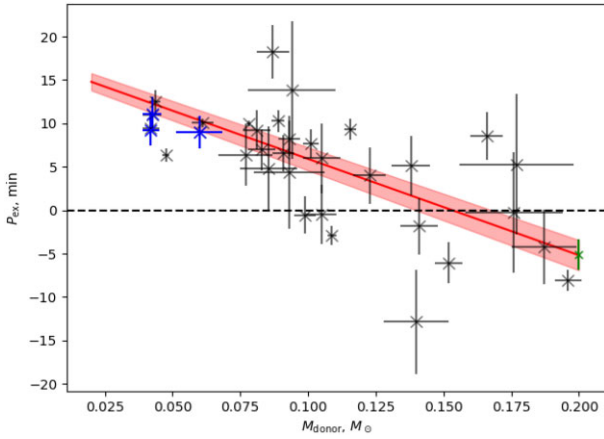


Figure 8. Showing period excess, P_{ex} (see Section 5.3) against the Knigge et al. (2011) ‘standard’ evolutionary track for short-period CVs from Fig. 7, excluding superhumpers, plotted as grey crosses. The three systems from this work are plotted as blue crosses. The solid red line shows the best-fitting straight line to the plotted data, and the shaded red band shows the 1σ region of the fit. The green cross and error bar show the predicted P_{ex} at $M_{\text{donor}} = 0.2 M_{\odot}$. The horizontal black dashed line is a guide to show $P_{\text{ex}} \equiv 0$.

The best-fitting parameters are a gradient of $-1.81 \pm 0.13 M_{\odot}/\text{h}$, and a y-intercept of $0.283 \pm 0.016 \text{ h}$. This gives $P_{\text{ex}} = -4.89 \pm 1.81 \text{ min}$ at $M_{\text{donor}} = 0.20 M_{\odot}$, where a CV emerges from the period gap, roughly consistent with $P_{\text{ex}} = 0$, and the data show a clear increase in P_{ex} towards lower M_{donor} .

We again stress that the only robust product of this analysis is the *sign of the gradient* of the $M_{\text{donor}} - P_{\text{ex}}$ relationship, and that its steepness and y-intercept are both subject to systematic errors that we cannot capture in the statistical errors given above. Despite this, the clear and statistically highly significant increase in P_{ex} towards low masses implies that additional AML has a larger effect on the donor at low masses.

The strength of gravitational braking falls with the total system mass, so we are left with three possibilities: the excess AML also declines in strength but more slowly than gravitational braking; excess AML is roughly constant across the range of M_{donor} ; or excess AML actually increases in strength towards lower M_{donor} . None of these options translate to the ‘optimal’ Knigge et al. (2011) models that adopt additional AML of the same form as gravitational braking.

We cannot convert our data to a more detailed AML prescription, as the donor radius and mass will be highly dependent on the mass-loss *history* of the system (Knigge et al. 2011). The donor star does not respond instantly to mass-loss, but adjusts on a thermal time-scale that is generally much longer than the mass-loss time-scale, so the degree of inflation a donor exhibits at a given mass will be affected by AML rates in the past. When a CV emerges from the period gap, the history is not significant as the donor has had ample time to adjust to the ‘correct’ radius for its mass, but as it evolves to lower M_{donor} , it will become more affected by the AML history of the system.

It is not currently possible to distinguish between proposed mechanisms for excess AML in CVs. However, an empirically determined, accurate AML prescription will help provide constraints for further exploration; the number of observations at the extremes of the donor track are now sufficient to begin to properly constrain the form of excess AML, but will require full evolutionary modelling with a focus on this aspect.

6 CONCLUSION

We contribute the component masses and radii, separations, white dwarf temperatures, and surface gravities of three new short-period CVs to the population of well-characterized CV observations, two of which have extremely low-mass donor stars, and one which appears to be in the process of evolving through the period minimum. We measure the T_{eff} of the white dwarf in SSSJ0522-3505 to be $\sim 10\,000 \text{ K}$ higher than is typical for a CV. We note that our derived temperature is quite uncertain, but we cannot confidently determine the origin of the discrepancy and summarize possible causes. All three of the newly modelled systems lie within 1σ of the ‘optimal’ model mass–radius evolutionary tracks from Knigge et al. (2011).

The ‘optimal’ tracks add an extra source of AML that takes the form of 1.5 times the gravitational braking. By examining the period excess between the growing set of observed CV donor radii and models, we demonstrate that this does not properly describe the missing AML. Rather than tracking the gravitational braking as the CV evolves to lower masses, we find that the excess AML grows in strength relative to gravitational losses as the donor shrinks. The degree of inflation of the donor should provide an empirical diagnostic for this excess AML. Deriving a more quantitative AML prescription is beyond the scope of this work, as it would require fitting detailed evolutionary models to observations, due to the degree of donor inflation having a complex relationship with the AML history of the system.

ACKNOWLEDGEMENTS

TRM acknowledges the support of the Science and Technology Facilities Council (STFC) grant STFC ST/T000406/1 and the Leverhulme Trust.

This work has made use of data from the European Space Agency (ESA) mission *Gaia* (<https://www.cosmos.esa.int/gaia>), processed by the *Gaia* Data Processing and Analysis Consortium (DPAC, <https://www.cosmos.esa.int/web/gaia/dpac/consortium>). Funding for the DPAC has been provided by national institutions, in particular the institutions participating in the *Gaia* Multilateral Agreement.

This research has made use of the NASA/IPAC Infrared Science Archive, which is funded by the National Aeronautics and Space Administration and operated by the California Institute of Technology.

We thank the anonymous referee for their careful reading of the paper, which greatly improved the quality of the results.

DATA AVAILABILITY

The data underlying this article will be shared on reasonable request to the corresponding author.

REFERENCES

- Allard F., Homeier D., Freytag B., 2012, in Richards M. T., Hubeny I., eds, Proc. IAU Symp. Vol. 282, From Interacting Binaries to Exoplanets: Essential Modeling Tools, p. 235
 Bergeron P., Wesemael F., Beauchamp A., 1995, *PASP*, 107, 1047
 Britt C. T. et al., 2015, *MNRAS*, 448, 3455
 Choi J., Dotter A., Conroy C., Cantiello M., Paxton B., Johnson B. D., 2016, *ApJ*, 823, 102
 Copperwheat C. M. et al., 2012, *MNRAS*, 421, 149
 Davis P. J., Kolb U., Willems B., Gänsicke B. T., 2008, *MNRAS*, 389, 1563
 Dhillion V. S. et al., 2007, *MNRAS*, 378, 825

Dhillon V. S. et al., 2016, in Evans C. J., Simard L., Takami H., eds, Proc. SPIE Conf. Ser. Vol. 9908, Ground-based and Airborne Instrumentation for Astronomy VI. SPIE, Bellingham, p. 99080Y

Dotter A., 2016, *ApJS*, 222, 8

Drake A. J. et al., 2008, *ApJ*, 696, 870

Foreman-Mackey D., Hogg D. W., Lang D., Goodman J., 2013, *PASP*, 125, 306

Gaia Collaboration, 2016, *A&A*, 595, A1

Gaia Collaboration, 2018, *A&A*, 616, A1

Garraffo C., Drake J. J., Alvarado-Gomez J. D., Moschou S. P., Cohen O., 2018, *ApJ*, 868, 60

Goliasch J., Nelson L., 2015, *ApJ*, 809, 80

Hameury J.-M., Menou K., Dubus G., Lasota J.-P., Hure J.-M., 1998, *MNRAS*, 298, 1048

Harrison T. E., 2016, *ApJ*, 833, 14

Hellier C., 2001, *Cataclysmic Variable Stars: How and Why They Vary*. Springer-Verlag, Berlin

Hogg D. W., Bovy J., Lang D., 2010, preprint ([arXiv:1008.4686](https://arxiv.org/abs/1008.4686))

Howell S. B., 2001, *PASJ*, 53, 675

Kato T. et al., 2009, *PASJ*, 61, S395

Kato T. et al., 2017, *PASJ*, 69, 75

King A., Kolb U., 1995, *ApJ*, 439, 330

Knigge C., 2006, *MNRAS*, 373, 484

Knigge C., Baraffe I., Patterson J., 2011, *ApJS*, 194, 28

Koester D., 2010, *Mem. Soc. Astron. Ital.*, 81, 921

Kolb U., 1993, *A&A*, 271, 149

Kolb U., Baraffe I., 1999, in Hellier C., Mukai K., eds, ASP Conf. Ser. Vol. 157, Annapolis Workshop on Magnetic Cataclysmic Variables. Astron. Soc. Pac., San Francisco, p. 273

Kolb U., King A., Ritter H., 1998, *MNRAS*, 298, L29

Lindegren L. et al., 2018, *A&A*, 616, A2

Luri X. et al., 2018, *A&A*, 616, A9

McAllister M. et al., 2019, *MNRAS*, 486, 5535

McAllister M. J. et al., 2017, *MNRAS*, 464, 1353

McCleery J. et al., 2020, *MNRAS*, 499, 1890

McDermott P. N., Taam R. E., 1989, *ApJ*, 342, 1019

Morin J., Donati J.-F., Petit P., Delfosse X., Forveille T., Jardine M. M., 2010, *MNRAS*, 407, 2269

Osaki Y., 1996, *PASP*, 108, 39

Paczynski B., Sienkiewicz R., 1981, *ApJ*, 248, L27

Pala A. F. et al., 2017, *MNRAS*, 466, 2855

Pala A. F. et al., 2020, *MNRAS*, 494, 3799

Panei J., Althaus L., Benvenuto O., 2000, *A&A*, 353, 970

Paterson K., Woudt P. A., Warner B., Breytenbach H., Gilligan C. K., Motsoaledi M., Thorstensen J. R., Worters H. L., 2019, *MNRAS*, 486, 2422

Patterson J., 1984, *ApJS*, 54, 443

Patterson J. et al., 2005, *PASP*, 117, 1204

Pearson K. J., 2007, *MNRAS*, 379, 183

Rappaport S., Joss P. C., Webbink R. F., 1982, *ApJ*, 254, 616

Rappaport S., Verbunt F., Joss P., 1983, *ApJ*, 275, 713

Ritter H., Kolb U., 2003, *A&A*, 404, 301

Savourey C. D., Littlefair S. P., Marsh T. R., Dhillon V. S., Parsons S. G., Copperwheat C. M., Steeghs D., 2012, *MNRAS*, 422, 469

Savourey C. D. J. et al., 2011, *MNRAS*, 415, 2025

Schreiber M. R., Zorotovic M., Wijnen T. P. G., 2016, *MNRAS*, 455, L16

Schwöpe A., Worpel H., Traulsen I., 2021, *A&A*, 646, A181

Smith J. A. et al., 2002, *AJ*, 123, 2121

Spark M. K., O'Donoghue D., 2015, *MNRAS*, 449, 175

Spruit H. C., Ritter H., 1983, *A&A*, 124, 267

Starrfield S., Iliadis C., Hix W. R., 2016, *PASP*, 128, 051001

Stehle R., Kolb U., Ritter H., 1997, *A&A*, 320, 136

Szkody P. et al., 2016, *AJ*, 152, 48

Taam R. E., Spruit H. C., 1989, *ApJ*, 345, 972

Townsley D. M., Bildsten L., 2003, *ApJ*, 596, L227

Townsley D. M., Bildsten L., 2004, *ApJ*, 600, 390

Townsley D. M., Gänsicke B. T., 2009, *ApJ*, 693, 1007

Tremblay P. E., Bergeron P., 2009, *ApJ*, 696, 1755

Tulloch S. M., Rodríguez-Gil P., Dhillon V. S., 2009, *MNRAS*, 397, L82

Warner B., 1995, *Ap&SS*, 232, 89

Wood M. A., 1995, in Koester D., Werner K., eds, *White Dwarfs*. Springer-Verlag, Berlin, p. 41

Wood J., Crawford C., 1986, *MNRAS*, 222, 645

Wood J. H., Irwin M. J., Pringle J. E., 1985, *MNRAS*, 214, 475

Zorotovic M., Schreiber M. R., 2020, *Adv. Space Res.*, 66, 1080

APPENDIX A: PHOTOMETRIC EXTRACTION AND CALIBRATION

The HiPERCAM data reduction pipeline (Dhillon et al. 2016) was used to perform debiasing and flat-field corrections on the raw frames. The software was also used for the extraction of aperture photometry, producing the flux in Analog-to-Digital Units, ADU, per frame of each source. A comparison star in the same image as the target was used to account for transparency variations, and standard stars from Smith et al. (2002) were used to transform the light curves from ADU to the SDSS $u'g'r'i'z'$ photometric system.

A1 Calculating atmospheric extinction coefficients

Atmospheric extinction was calculated using the longest continuous ULTRACAM observation available within 3 d of the target observations. The atmospheric extinction values are reported in Table A1. No suitable observation was available in 2020 January, so the average of the coefficients on 2018 October 14 and 2019 September 30 was used. Aperture photometry was extracted for five sources in these long observations, and the instrumental magnitude, m_{inst} , versus airmass, χ , was fit with a straight line for each source. The gradients of these lines are the atmospheric extinction coefficients, k_{ext} , for the relevant band, and the y-intercept is the instrumental magnitude of that object above the atmosphere, $m_{\text{inst},0}$:

$$m_{\text{inst}} = m_{\text{inst},0} + \chi k_{\text{ext}}.$$

A2 Transformations between filter systems

The ULTRACAM photometric system previously matched the SDSS reasonably closely; however, in early 2019 it was upgraded and now uses an SDSS-like filter system with higher efficiency bandpasses, referred to as Super SDSS. There are three optical paths that are relevant:

- (i) SDSS filters, u', g', r', i', z' ;
- (ii) ULTRACAM SDSS, NTT, $u_{\text{reg}}, g_{\text{reg}}, r_{\text{reg}}, i_{\text{reg}}, z_{\text{reg}}$;
- (iii) ULTRACAM Super SDSS, NTT, $u_{\text{sup}}, g_{\text{sup}}, r_{\text{sup}}, i_{\text{sup}}, z_{\text{sup}}$.

We aim to place our photometry in the SDSS $u'g'r'i'z'$ system, as this is the system later used by the white dwarf atmospheric models.

Table A1. Atmospheric extinction coefficients for La Silla, derived from ULTRACAM/NTT observations.

Date of observation	Airmass range	Band	k_{ext}
14 Oct 2018	1.30–1.98	u_{reg}	0.4476
		g_{reg}	0.1776
		r_{reg}	0.0861
30 Sept 2019	1.03–1.63	u_{sup}	0.4867
		g_{sup}	0.1803
		r_{sup}	0.0713

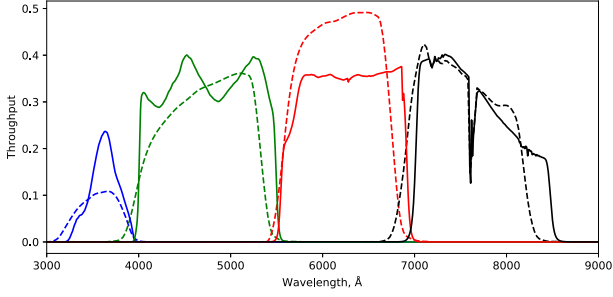


Figure A9. The differences in photometric throughput for SDSS filter system (dotted lines), and ULTRACAM Super SDSS filters, for ULTRACAM mounted on the NTT (solid lines). Blue: u bands, green: g bands, red: r bands, black: i bands. Both throughputs include atmospheric extinction of $\chi = 1.3$.

The u_{reg} , g_{reg} , r_{reg} , i_{reg} filters were sufficiently similar to standard SDSS filters that the uncorrected magnitudes of standard reference stars from Smith et al. (2002) could be used to calibrate absolute photometry without issue. However, with the new filters, there was concern that the different shapes of the sensitivity curve, particularly in the u' band, differ enough from the standard filters to cause issues with our photometric calibration. Fig. A9 illustrates the change in throughput between the SDSS photometric system, and the Super SDSS filters, on ULTRACAM on the NTT.

To perform the colour corrections, the following equation for the magnitude of a star was used, using the g' band as an example:

$$g' = g_{\text{inst}} + \chi k_{\text{ext}} + g_{\text{zp}} + c_{g,\text{sup}}(g' - r'), \quad (\text{A1})$$

where g_{zp} is the zero-point, $g_{\text{inst}} = -2.5 \log(\text{ADU}/t_{\text{exp}})$ for an exposure time of t_{exp} , and $c_{g,\text{sup}}$ is the colour term correction gradient.

The optical path of each system was simulated using the `pysynphot` package, with measured throughputs of all ULTRACAM components in the optical path. Models from Dotter (2016) and Choi et al. (2016) were used to generate the T_{eff} and $\log(g)$ values of an 8.5 Gyr isochrone for main-sequence stars with masses from 0.1 to 3 M_{\odot} . These span from $\log(g) = 3.73 \rightarrow 5.17$, and $T_{\text{eff}} = 2900\text{K} \rightarrow 10\,300\text{K}$. The Phoenix model atmospheres (Allard, Homeier & Freytag 2012) were used to generate model spectra of each mass, which was then folded through each optical path to calculate an AB magnitude. In addition, white dwarf models with $\log(g) = 8.5$ were similarly processed (Tremblay & Bergeron 2009; Koester 2010), to assess the impact of the different spectral shape on the resulting colour terms.

We synthesized the colour terms between the SDSS and ULTRACAM Super SDSS systems, e.g. $g' - g_{\text{sup}}$, for each model atmosphere. These data were plotted against SDSS colours, i.e. $(u' - g')$, $(g' - r')$, $(g' - i')$, and a straight line was fit to the colour relationship. In the example case of $g' - g_{\text{sup}}$, this would be

$$g' = g_{\text{sup}} + g_{\text{zp}} + c_{g,\text{sup}}(g' - r').$$

Note, we ignore the effects of secondary extinction. These relationships are shown in Fig. A10 for all four ULTRACAM filters used to observe these CVs, and Table A2 contains the coefficients of each colour term. $(u' - g')$ was used to correct u magnitudes, $(g' - r')$ was used to correct g and r magnitudes, $(g' - i')$ was used to correct the i band. These colour corrections are not generally the same for main-sequence stars and white dwarfs, though the colours of the white dwarfs presented in this work are all such that the discrepancy is of the order of a few per cent, and is considered negligible.

A3 Calculating comparison star magnitudes

Equation (A1) was used to calculate the zero points in each band from the standard star, for the SDSS photometric system. The comparison star SDSS magnitudes are then determined. As the colour term corrections are dependent on SDSS colours, an iterative approach was used to converge on these values. The SDSS magnitudes are related to the instrumental magnitudes by:

$$\begin{aligned} u' &= u_{\text{inst},0} + u_{\text{zp}} + c_{u,\text{sup}}(u' - g') \\ g' &= g_{\text{inst},0} + g_{\text{zp}} + c_{g,\text{sup}}(g' - r') \\ r' &= r_{\text{inst},0} + r_{\text{zp}} + c_{r,\text{sup}}(g' - r'). \end{aligned}$$

Initially, u' , g' , r' magnitudes are set equal to the instrumental magnitudes, and a new set of u' , g' , r' magnitudes are calculated. The new values are then used to repeat the calculation until a new iteration produces no change, typically after ~ 4 loops. For the data taken with u_{sup} , g_{sup} , i_{sup} filters, the process is identical but replaces r with i .

A4 Producing a flux-calibrated target light curve

Finally, the target light curves can be calculated. We need to both correct the target star light curve for transparency variations, and convert from counts to calibrated fluxes. As we are producing a flux-calibrated light curve in the SDSS photometric system using a significantly different photometric system, the simple ADU ratio between the target and comparison is insufficient. Consider the target star g' magnitude and flux, g' , F^t , and comparison star g' magnitude and flux, g^c , F^c :

$$\begin{aligned} g^t &= g_{\text{inst},0}^t + g_{\text{zp}} + c_{g,\text{sup}}(g' - r')^t \\ g^c &= g_{\text{inst},0}^c + g_{\text{zp}} + c_{g,\text{sup}}(g' - r')^c, \end{aligned}$$

since

$$g^t - g^c = -2.5 \log\left(\frac{F^t}{F^c}\right),$$

we can write

$$\begin{aligned} \frac{F^t}{F^c} &= 10^{-0.4(g_{\text{inst},0}^t - g_{\text{inst},0}^c)} \cdot 10^{-0.4c_{g,\text{sup}}((g' - r')^t - (g' - r')^c)} \\ \frac{F^t}{F^c} &= \frac{\text{ADU}^t}{\text{ADU}^c} \cdot K^{t,c} \end{aligned}$$

where $K^{t,c} = 10^{-0.4c_{g,\text{sup}}((g' - r')^t - (g' - r')^c)}$. This accounts for differences in wavelength response between the two systems when calculating the flux ratio, and is applied to each frame. The $(g' - r')^t$ magnitudes are calculated using a sigma-clipped mean instrumental magnitudes computed from all frames in the observation. In practice, the factor $K^{t,c}$ varies from ~ 1.0 to 1.1 across the three systems.

ASASSN-16kr was observed in both the standard SDSS filters in 2018, and the super SDSS filters in 2019. This presented an opportunity to compare the corrected 2019 data with the fluxes observed in 2018. Additionally, both ASASSN-16kr and SSSJ0522-3505 use multiple standard stars across observations, which should agree if the calibration has been done correctly. In all cases, the flux-calibrated light curves were similar and the white dwarf colours consistent, suggesting an accurate flux calibration. See Appendix B for flux-calibrated light curves.

To account for residual error in flux calibration, we add a 3 per cent systematic error in quadrature to the white dwarf fluxes when fitting for the effective temperature.

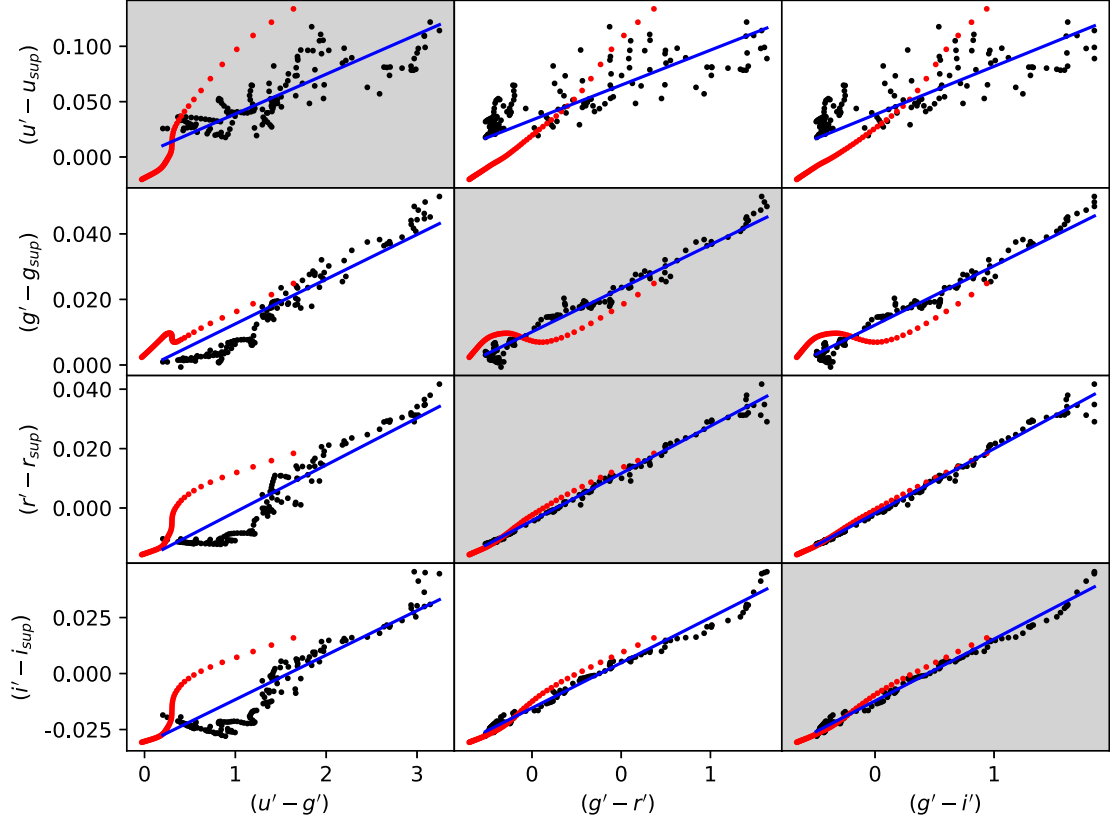


Figure A10. The difference between the classic SDSS photometric system, and the ULTRACAM SuperSDSS filters on the NTT, as a function of SDSS colours, are calculated for model atmospheres. Red points are Koester white dwarf models, black points are Phoenix main-sequence model atmospheres, and the blue line is the best-fitting straight line to both data sets. When applying colour corrections, the highlighted relations were used.

Table A2. Colour term best-fitting lines from Fig. A10. The data are modelled by equations of the form $(u' - u_s) = \phi + c_u(u' - g')$, with c_u being the relevant colour gradient.

Correction	Diagnostic	y-intercept, ϕ	Colour gradient
$(u' - u_s)$	$(u' - g')$	0.003	0.036
	$(g' - r')$	0.033	0.063
	$(g' - i')$	0.038	0.044
$(g' - g_s)$	$(u' - g')$	-0.001	0.014
	$(g' - r')$	0.010	0.027
	$(g' - i')$	0.012	0.018
$(r' - r_s)$	$(u' - g')$	-0.017	0.016
	$(g' - r')$	-0.004	0.032
	$(g' - i')$	-0.002	0.022
$(i' - i_s)$	$(u' - g')$	-0.031	0.020
	$(g' - r')$	-0.015	0.040
	$(g' - i')$	-0.012	0.028

A5 Ephemeris data

ASASSN-16kr has existing ephemeris data in the literature (Kato et al. 2017), whereas SSSJ0522-3505 and ASASSN-17jf were reported with tentative period estimates. These were used as starting points, and eclipse times from this work were used to refine the T_0 and P for all three systems. Only ULTRACAM eclipse timings were used to calculate the ephemerides in this paper.

To calculate the time of white dwarf mid-eclipse for each observation, the numerical derivative of the flux was fit with a double-Gaussian model, as described in Wood, Irwin & Pringle (1985). Ideally, the derivative shows a negative peak at white dwarf ingress, and a symmetrical positive peak at egress, and each would be equidistant from the white dwarf mid-eclipse time, T_{ecl} . By fitting the double-Gaussian model to a smoothed, numerical derivative of the light curve using an MCMC method using a Gaussian process to evaluate the log-likelihood, we obtain T_{ecl} with uncertainties for each eclipse. These values are reported in Table 2.

For each observed T_{ecl} , its eclipse number N (the number of eclipses since T_0) could unambiguously be determined from prior ephemeris data. An MCMC algorithm was used to fit a straight line model to the independent variable N and dependent variable T_{ecl} , with a gradient P and intercept T_0 . The model accounts for potential systematic differences in timing accuracy between instruments by also having variable error scale factors applied to all eclipses observed with a specific instrument, e.g. the timing reported for eclipses observed with ULTRACAM may be systematically offset from reality, and the errors associated with those observations might need to be larger than reported to be consistent with data from other instruments. The prior distribution assumed for these error factors was log-uniform ranging from 0.01 to 100, which favours the smallest factor consistent with the data. The values of N for each system were chosen to minimize the covariance between T_0 and P . The results of this ephemeris fitting are included in Table 1.

APPENDIX B: LIGHT CURVES

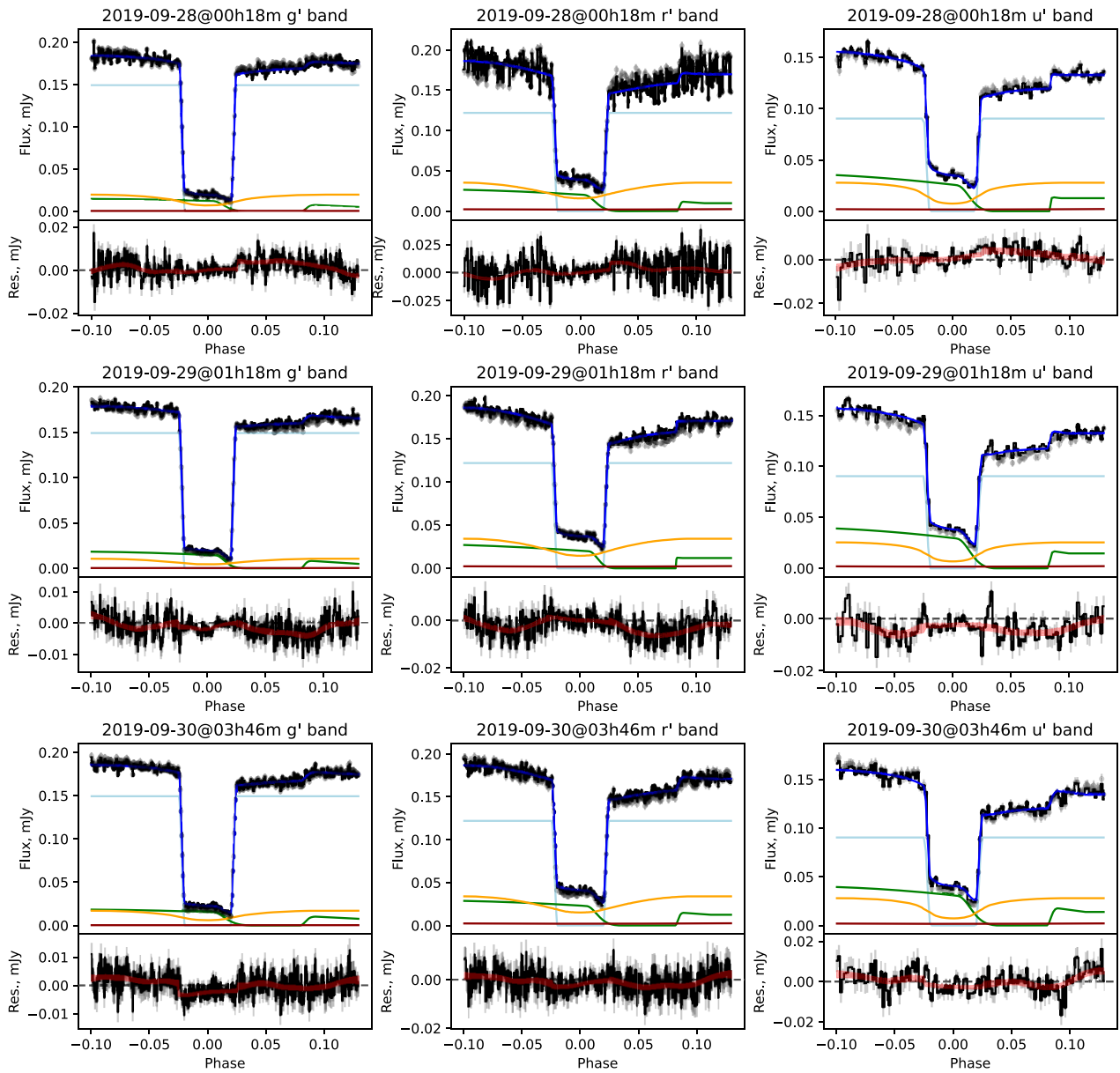


Figure B3. ASASSN-16kr light-curve models (cont.).

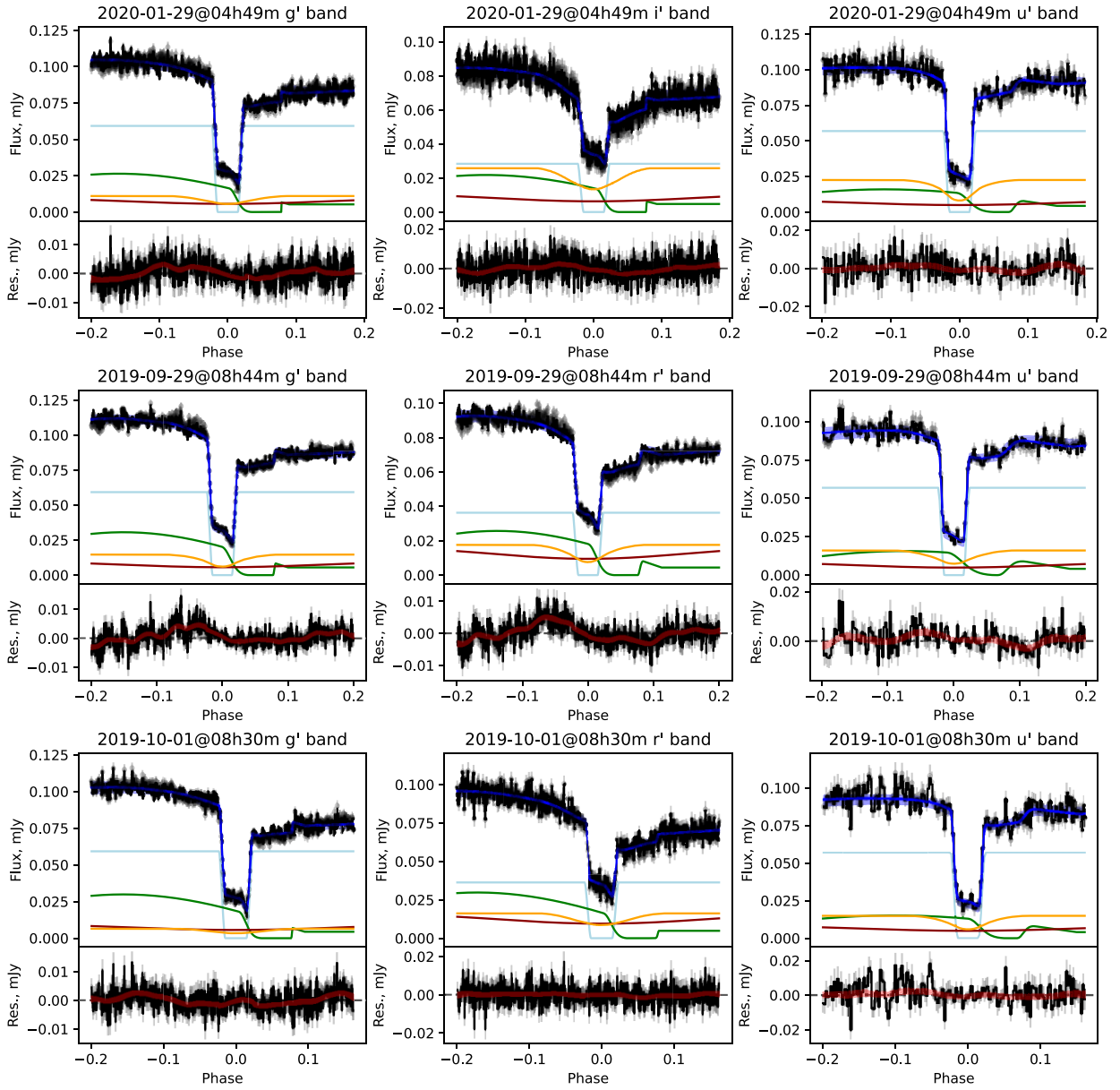


Figure B4. SSSJ0522-3505 light-curve models. Symbols are the same as Fig. B11.

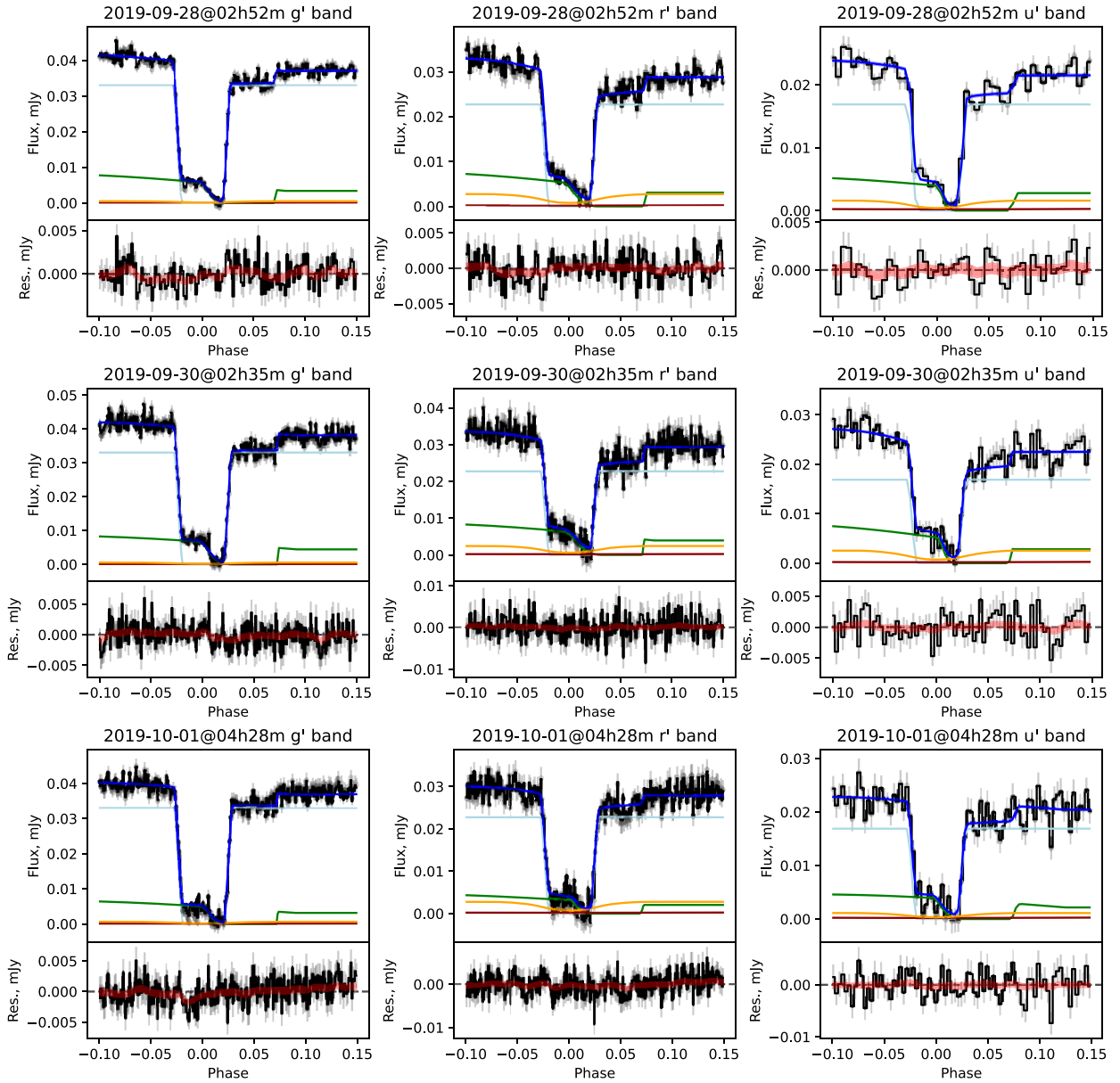


Figure B11. ASASSN-17jf light-curve models. *Top*: grey points are the observed flux; black line is the observed flux, with the mean Gaussian process sample subtracted; the dark blue line is the mean light-curve model, and the blue band is the standard deviation on this in the MCMC chain. The components of the model are also shown: the light blue line is the white dwarf flux, green line is the bright-spot, orange line is the disc, and the red line is the donor. *Bottom*: The residuals between the data and model are plotted as the black line, with grey error bars. The Gaussian process 1σ region is shown as a red band.

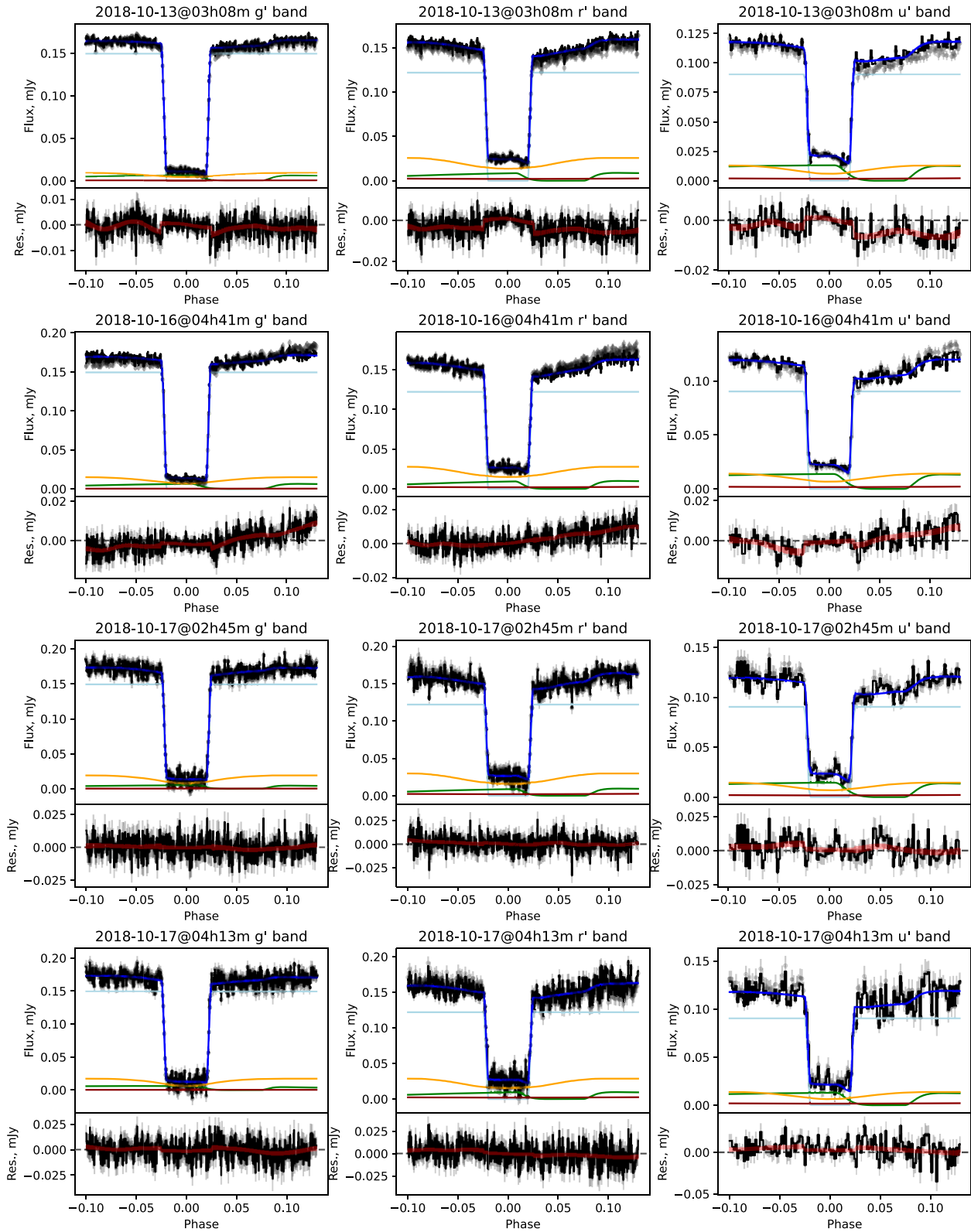


Figure B12. ASASSN-16kr light-curve models. Symbols are the same as Fig. B11.

This paper has been typeset from a \LaTeX file prepared by the author.